DFT normal modes of vibration of the Au_{20} cluster

B. Molina, J.R. Soto, and A. Calles
Facultad de Ciencias, Universidad Nacional Autónoma de México,
Apartado Post.al 70-646, 04510 México D.F., México.
Members of UNAM Nanotechnology Project (PUNTA).

Recibido el 7 de mayo de 2008; aceptado el 23 de mayo de 2008

The vibrational spectrum of the tetrahedral Au_{20} cluster was calculated using density functional theory (DFT) with two different approximations: the hybrid-B3LYP and GGA-BP86. The normal modes of vibration obtained were classified according to the irreducible representations of the T_d group. The calculated vibrational frequencies were tabulated to be compared with experimental data when they became available.

Keywords: Au_{20}; metallic cluster; normal modes of vibration.

El espectro vibracional del cúmulo tetraédrico Au_{20} fue calculado mediante la teoría del funcional de la densidad (DFT) dentro de dos aproximaciones diferentes: la híbrida B3LYP y la GGA-BP86. Los modos normales de vibración obtenidos fueron clasificados de acuerdo a las representaciones irreducibles del grupo T_d. Las frecuencias vibracionales calculadas fueron tabuladas para su comparación con datos experimentales cuando estén disponibles.

Descriptores: Au_{20}; cúmulos metálicos; modos normales de vibración.

PACS: 71.15.Md; 33.20.Sl; 61.46.Bc

1. Introduction

The tetrahedral 20-gold cluster (T_d-Au_{20}) is perhaps the most widely studied gold cluster due to its high symmetry. It was discovered through a combined experimental and theoretical work by Li *et al.* [1]. Its tetrahedral geometry, predicted from a density functional theory (DFT) calculation, has been described as a piece of fcc bulk gold, with the twenty gold atoms on its surface and each of its four faces forming a plane (111). The constructed polyhedra is a tetrahedral pyramid with its four corners being low coordination sites [1,2] (see Au^a sites in Fig. 1). These kinds of sites are preferred for CO adsorption on gold clusters in the gas phase [3]. Zhang *et al.* [4] synthesized Au_{20} in solution, coordinated with eight ligands PH_3: four located at the apexes of the cluster and the remaining four connected to the face-centered atoms (Au^f sites in Fig. 1). The new complex molecule definitely shows compatibility with a tetrahedral symmetry. Theoretical studies on T_d-Au_{20} suggest that indeed this cluster presents catalytic characteristics for CO and O_2 at low coordination sites [5]. Experimentally, Neumaier *et al.* [6] report room temperature CO adsorption on isolated gold cluster cations and especially for Au_{20}^{+1} show the existence of four sites with similar adsorption rate constants. However, Veldeman *et al.* [7] do not report a particularly high reactivity for neutral Au_{20} towards CO.

The structural stability is another interesting feature of this cluster. Actually, it is well known that the small gold clusters undergo a dynamic structural fluxionality, changing their geometry easily during chemical reactions [8]. Nevertheless, from photoelectron spectroscopy, Li *et al.* showed that T_d-Au_{20} presents a wide HOMO-LUMO gap (1.77 eV), *i.e.* 0.2 eV larger than that of C_{60}), which would be a high structural stability indicator.

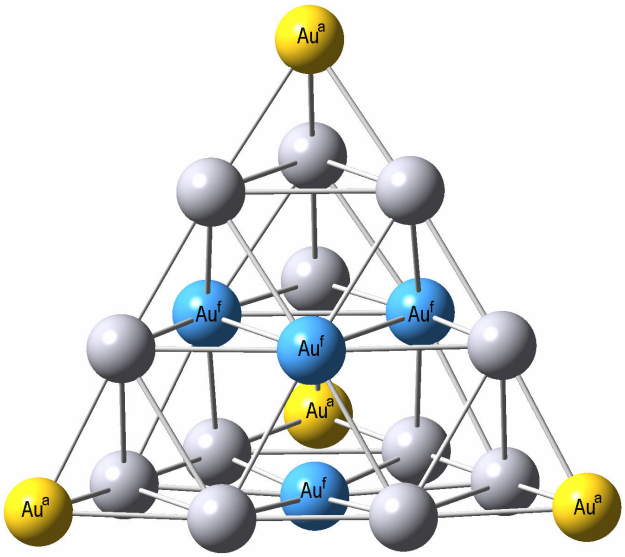

FIGURE 1. Tetrahedral structure of Au_{20} showing its three non-equivalent sites: Au^a, Au^f and Au^e corresponding to apexes, face centers and edges respectively (the last ones corresponding to the empty spheres in figure).

On the other hand, it can be seen that the spectrum of theoretical and experimental studies around T_d-Au_{20} is broad; for instance, the T_d-Au_{20} cluster has been studied theoretically associated with surface-enhanced Raman scattering by pyridine [9]. Furthermore, this cluster has also been proposed for application in molecular opto-electronic devices and monolayer film materials because theoretically it has a remarkably large static first hyperpolarizability [10]. In addition, several of its ions have been obtained ($Au_{20}^{\pm\gamma}$, γ=1,2,3) [11], but there are few theoretical studies on them.

Recently, in Au_n clusters, the use of vibrational spectra has been proposed as an efficient tool to resolve between dif-

ferent isomers [12]. About the T_d-Au_{20} cluster, Kryachko and Remacle [13] have reported its lowest and highest vibrational frequencies using different approximations. Before, Carnalla *et al.* [14] provided the frequency spectrum for the unsymmetrical Au_{20} cluster. The experimental frequency spectrum of the T_d-Au_{20} cluster is not yet available because it must be obtained through infrared or Raman optical spectroscopies, or using inelastic neutron dispersion carried out when the material is in solid-phase. However, there are many experimental efforts to achieve the self-assembly of gold nanoparticles in periodic arrangements through interligand interaction [15]. Thus, the self-assembly of ordered T_d-Au_{20} and therefore, the experimental frequency spectrum for T_d-Au_{20}, is only a question of time.

Briefly, we can mention some features concerning the vibrational spectrum of the T_d-Au_{20} cluster. The normal modes of vibration of this cluster may be classified according to their symmetry using group theoretical techniques. There are 60 degrees of freedom for the Au_{20} cluster. Three of these degrees correspond to translations and three to rotations, leaving 54 vibrational degrees of freedom. Since tetrahedral symmetry gives rise to a large number of degenerate modes, only 23 distinct mode frequencies are expected for the T_d-Au_{20} cluster:

$$\Gamma_{vib} = 4A_1 + A_2 + 5E + 5T_1 + 8T_2. \quad (1)$$

The symmetry labels (*e.g.* T_1, E) refer to irreducible representations (IR's) of the tetrahedral point group T_d.

Group theory, furthermore, indicates that nine of the 23 normal modes of vibration are Raman-active ($4A_1$ + 5E) in the first order, eight are both infrared and Raman-active ($8T_2$) in the first order, and the remaining six are optically silent.

In this work, we present the results of DFT calculations for the normal modes of vibration and the respective frequencies of the T_d-Au_{20} cluster, classified according to their symmetry group.

2. Methodology

Density functional theory calculations were carried out to optimize the geometry of the T_d-Au_{20} cluster. The exchange and correlation interactions were treated through GGA-BP86 and hybrid-B3LYP approximations. The GGA-BP86 approximation uses the gradient-corrected exchange-energy functional proposed by Becke [16] and the gradient-corrected correlation-energy functional proposed by Perdew [17]. The hybrid-B3LYP approximation was formulated by Becke [18] and includes a mixture of Hartree-Fock and DFT exchange energy functionals. We have used the relativistic effective core potential LANL2DZ basis set [19] to describe the gold atom. This basis set models the gold atom as being composed of 19 valence electrons plus a relativistic core potential centered at the gold nucleus. In order to improve the SCF convergence, an accuracy of 10^{-4} Hartrees was selected for energy and, for the optimization process, a gradient maximum limit of 10^{-5} Hartrees/Bohr. Analytical second derivatives were performed in order to obtain the Hessian of T_d-Au_{20}. Gaussian 03 [20] was employed for all the calculations.

3. Results and discussion

The geometry of the tetrahedral Au_{20} cluster is characterized by five distinct Au-Au distances between the three nonequivalent sites (Au^a, Au^f, and Au^e, with the last of these corresponding to the empty spheres in Fig. 1). For Au_{20}, the highest occupied molecular orbital (HOMO) is two-fold degenerate with e IR, while the lowest unoccupied molecular orbital (LUMO) is three-fold degenerate with t_2 IR. The corresponding closed-shell total electronic state symmetry is the completely symmetrical A_1 IR with a large HOMO-LUMO gap. If we compare our HOMO-LUMO energy gap and bond length results in T_d-Au_{20} with those reported by Li *et al.* (see Table I, third row), it can be concluded that the BP86 functional obtains good agreement with the experiment and gives us better predictions than the B3LYP functional. In fact, recently Kryachko and Remacle carried out density functional calculations using BP86, PW91, PBE and B3LYP functionals with two basis (LANL2DZ and SSD) on T_d-Au_{20}. Table I includes their results for BP86/LANL2DZ and B3LYP/LANL2DZ and can be compared respectively with the results of this work. The power of prediction of BP86 and B3LYP functionals has been tested before in diatomic molecules formed from alkali metals (Li, Na,K) and noble transition metals (Ag, Cu, Au) [21], and BP86 was better than B3LYP.

TABLE I. HOMO-LUMO energy gap (ΔE_{HL}), HOMO energy, electronic configuration, and Au-Au distances for T_d-Au_{20} employing different DFT approximations as compared with Ref. 13 and experiment [1].

Method	ΔE_{HL} (eV)	HOMO (eV)	configuration	Au-Au distances (Å)
BP86	1.92	-6.03	$(t_2)^6(e)^4(t_2)^0$	2.71, 2.76, 2.87, 3.01, 3.13
B3LYP	2.96	-6.41	$(t_2)^6(e)^4(t_2)^0$	2.73, 2.79, 2.91, 3.08, 3.21
KR-BP86 [13]		-6.02		2.71, 2.76, 2.86, 3.01
KR-B3LYP [13]		-6.40		2.73, 2.80, 2.91, 3.08
Theo/Exp. [1]	1.77		$(t_2)^6(e)^4(t_2)^0$	2.68, 2.71, 2.83, 2.97, 3.12

TABLE II. The Au_{20} vibrational spectra in cm^{-1} calculated in the present work using the DFT-BP86 and B3LYP approximations. The irreducible representation (IR) of each mode is given in the first column. The KR1 y KR2 columns correspond to the BP86/LANL2DZ and B3LYP/LANL2DZ respectively of Ref. 13.

IR	BP86	KR1	BLYP	KR2	IR	BP86	KR1	BLYP	KR2
$1T_1$	29.13	28	26.42	26	$5T_2$	72.94		65.21	
$1T_2$	33.29		29.94		$2A_1$	81.24		74.70	
1E	35.44		32.52		$4T_1$	89.36		80.22	
$2T_2$	43.46		39.47		$3A_1$	97.37		88.97	
2E	44.51		41.34		$5T_1$	106.61		93.74	
$1A_2$	47.14		44.66		4E	109.59		97.45	
$2T_1$	50.05		44.94		$6T_2$	114.61		102.94	
$3T_2$	55.04		51.47		$7T_2$	129.75		119.01	
3E	55.40		51.95		5E	159.18		149.67	
$1A_1$	57.33		47.81		$8T_2$	165.68		155.69	
$3T_1$	59.73		54.79		$4A_1$	172.35	172	162.22	161
$4T_2$	66.56		58.90						

The calculated values for all of the 23 mode frequencies are displayed in Table II for both approximations (BP86 and B3LYP) where each frequency level is identified according to its appropriate irreducible representation. We can see that the frequencies predicted by BP86 are slightly greater than those predicted by B3LYP (the maximum and minimum difference

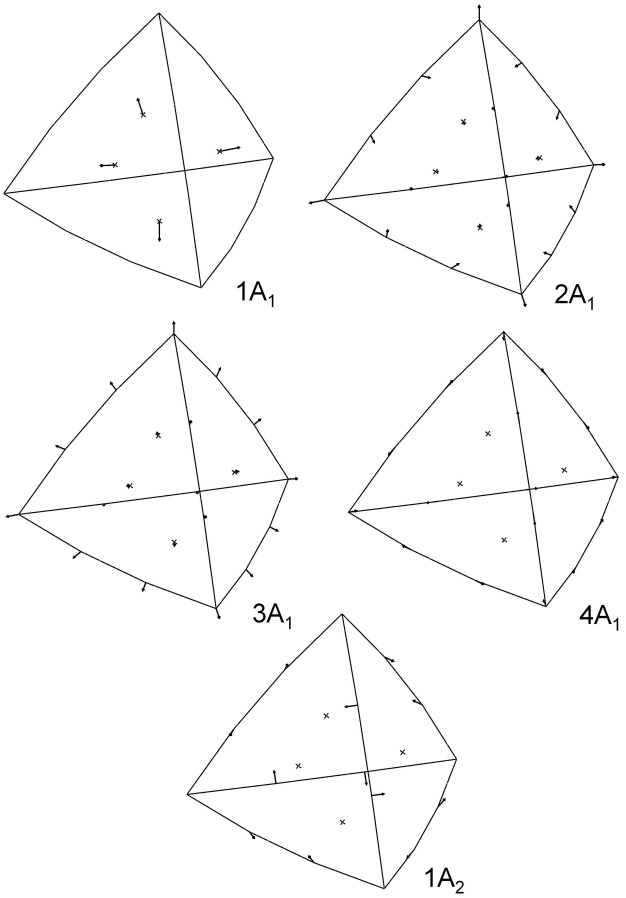

FIGURE 2. Schematic diagram of normal mode displacements for the four nondegenerate modes A_1 and A_2 in Au_{20}.

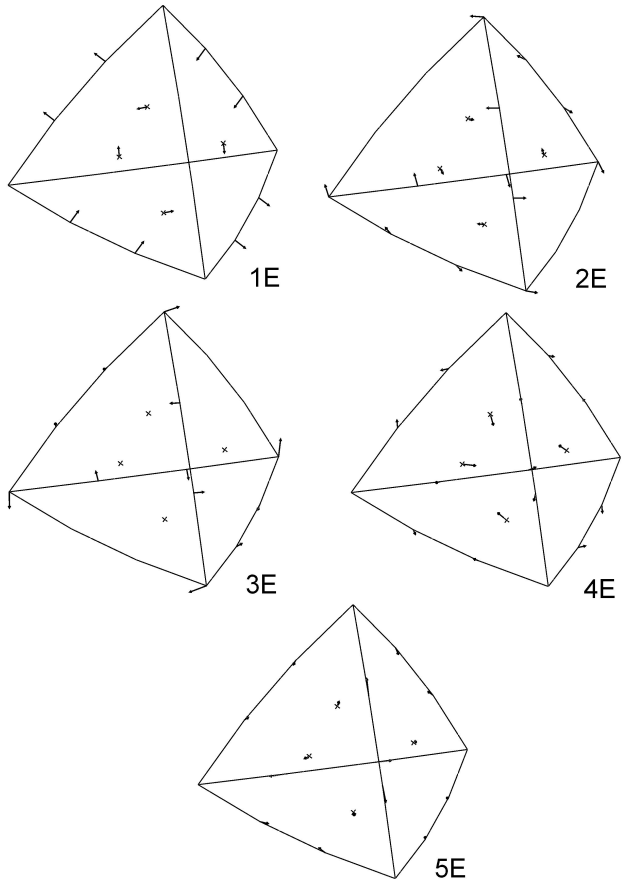

FIGURE 3. Schematic diagram of normal mode displacements for the five E modes in Au_{20}.

are 12.87 and 2.48 cm^{-1} respectively) and the increasing order of the frequencies is only broken in the $1A_1$ representation for B3LYP with respect to BP86 results. Our BP86 and B3LYP lowest and highest vibrational frequencies are very close to the corresponding frequencies calculated by Kryachko and Remacle with their respective functionals, as can be seen also in Table II.

In Fig. 2 we display eigenvectors for the four A_1 and one A_2 modes. These non-degenerate modes, because of their higher symmetry, are easier to visualize. In the $1A_1$ mode only the face-centered atoms are displaced perpendicularly to the face planes. The lower non-degenerate mode ($1A_2$) displaces atoms only at the edges, not at the vertices or face centers. The $3A_1$ Raman breathing mode with a frequency of approximately 97 cm^{-1} (BP86) or 89 cm^{-1} (B3LYP) involves identical radial displacements for all 20 gold atoms, whereas the higher frequency $4A_1$ mode involves only tangential displacements of the atoms at the edges.

In Figs. 3-5 we show some representative modes of each degenerate IR from the DFT-BP86 approximation. There is a general tendency of the higher frequency modes to have displacements that are more tangential in character than those at lower frequencies, except for two intermediate-frequency modes ($2T_1$ and $4T_1$). There is at least one mode of each IR whose eigenvectors are nulls at the face-centered atoms ($4A_1$, 3E, $5T_2$, $1A_2$, and $4T_1$) and with the exception of T_2 IR, there is at least one mode of each IR whose eigenvectors are nulls at the triangle vertices ($1A_1$, 4E, 5E, $1A_2$, and $5T_1$).

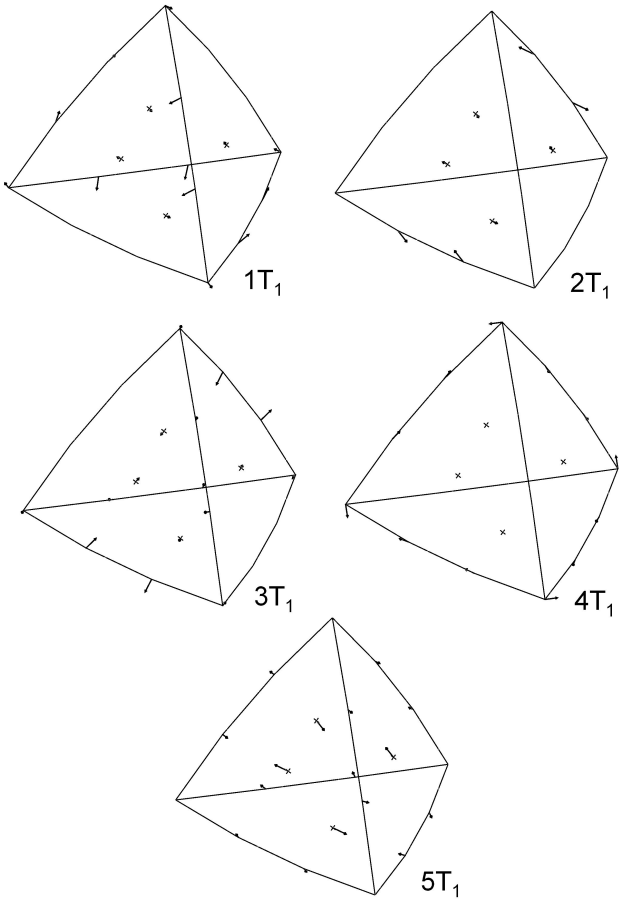

FIGURE 4. Schematic diagram of normal mode displacements for the five T_1 modes in Au_{20}.

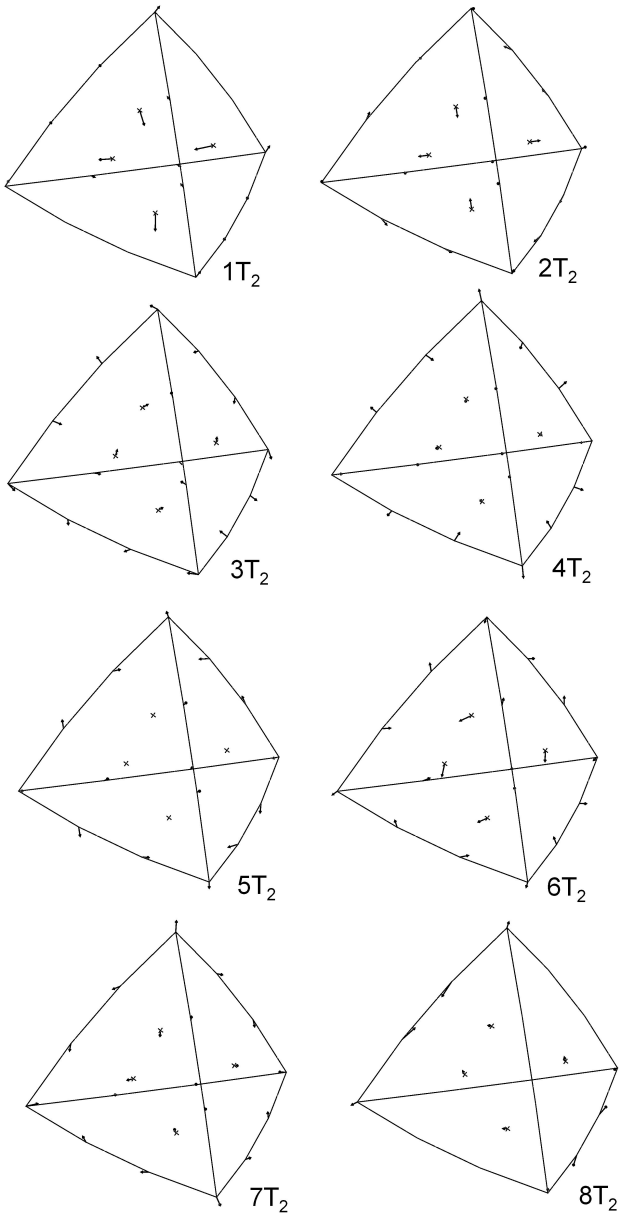

FIGURE 5. Schematic diagram of normal mode displacements for the eight T_2 modes in Au_{20}.

4. Conclusions

We use DFT with restricted B3LYP and BP86 to optimize the T_d-Au_{20} structure and to obtain its frequency spectrum. The resulting geometric and electronic structures are in agreement with other first principle calculations. The lowest and highest frequency values, as we mentioned previously, are very close to other similar calculations recently reported. The present calculation of the frequency spectrum is a prediction to be confirmed when the experimental data become available.

The Hessian matrix, calculated to obtain the normal modes of vibration in this work, can be useful in molecular dynamics simulations which can find a dependency of the gold-cluster-assisted catalytic processes on temperature.

Acknowledgments

We are grateful for the computer facilities of Dirección General de Servicios de Cómputo Académico and the Nanotechnology project (PUNTA) of the Universidad Nacional Autónoma de México and B. Molina acknowledge the support of Dirección General de Asuntos del Personal Académico, UNAM.

1. J. Li, X. Li, H.-J. Zhai, and L.-S. Wang, *Science* **299** (2003) 864.
2. a) W. Fa, C. Lou, and J. Dong, *Phys. Rev. B* **72** (2005) 205428; b) E. Aprà, R. Ferrando, and A. Fortunelli, *Phys. Rev. B* **73** (2006) 205414; c) J.C. Idrobo *et al.*, *Phys. Rev. B* **76** (2007) 205422; d) R.B. King, Z. Chen, and P. von R. Schleyer, *Inorg. Chem.* **43** (2004) 4564; e) E.M. Fernández, J.M. Soler, I.L. Garzón, and L.C. Balbás, *Phys. Rev. B* **70** (2004) 165403; f) B.S. de Bas, M.J. Ford, and M.B. Cortie, *J. Mol. Struc.-TheoChem* **686** (2004) 193.
3. N. Lopez *et al.*, *J. Catal.* **223** (2004) 232.
4. H.-F. Zhang *et al.*, *J. Phys. Chem. B* **108** (2004) 12259.
5. A. Shiga and M. Haruta, *Appl. Catal. A-Gen.* **291** (2005) 6.
6. M. Neumaier, F. Weigend, O. Hampe, and M.M. Kappes, *J. Chem. Phys.* **122** (2005) 104702.
7. N. Veldeman, P. Lievens, and M. Andersson, *J. Phys. Chem. A* **109** (2005) 11793.
8. H. Häkkinen, S. Abbet, A. Sanchez, U. Heiz, and U. Landman, *Angew. Chem. Int. Edit.* **42** (2003) 1297.
9. C.M. Aikens and G.C. Schatz, *J. Phys. Chem. A* **110** (2006) 13317.
10. K. Wu, J. Li, and C. Lin, *Chem. Phys. Lett.* **388** (2004) 353.
11. a)A. Dreuw and L.S. Cederbaum, *Chem. Rev.* **102** (2002) 181; b) J. Ziegler *et al.*, *Int. J. Mass Spectrom.* **202** (2000) 47; c) U. Näher, S. Børnholm, S. Frauendorf, F. Garcias, and C. Guet, *Phys. Rep.* **285** (1997) 245; d) A. Herlert, and L. Schweikhard, *Int. J. Mass Spectrom.* **229** (2003) 19; e) C. Stoermer, J. Friedrich, and M.M. Kappes, *Int. J. Mass Spectrom.* **206** (2001) 63; f) A. Herlert, S. Krückeberg, L. Schweikhard, M. Vogel, and C. Walther, *J. Electron Spectrosc.* **106** (2000) 179; g) C. Yannouleas and U. Landman, *Rhys. Rev. B* **61** (2000) R10587; h) A. Herlert, S. Krückeberg, L. Schweikhard, M. Vogel, and C. Walther, *Phys. Scr.* **T80** (1999) 200; i) J. Ziegler *et al.*, *Hyperfine Interact.* **115** (1998) 171.
12. W. Fa and J. Dong, *Appl. Phys. Lett.* **89** (2006) 013117.
13. E.S. Kryachko and F. Remacle, *Int. J. Quantum Chem.* **107** (2007) 2922.
14. S. Carnalla, A. Posada, and I.L. Garzón, *Nanostruct. Mater.* **3** (1993) 385.
15. X.Q. Wang, C.Z. Wang, and K.M. Ho, *Phys. Rev. B* **51** (1995) 8656.
16. A.D. Becke, *Phys. Rev. A* **38** (1988) 3098.
17. J.P. Perdew, *Phys. Rev. B* **33** (1986) 8822.
18. A.D. Becke, *J. Chem. Phys.* **98** (1993) 5648.
19. P.J. Hay and W.R. Wadt, *J. Chem. Phys.* **82** (1985) 270.
20. M.J. Frisch *et al.*, *Gaussian03*, Gaussian Inc. Wallingford, CT. 2004.
21. G.S.M. Tong and A.S.C. Cheung, *J. Phys. Chem. A* **106** (2002) 11637.